**PIER C**

# Analysis and Optimization of the Electromagnetic Characteristics of a Built-in Combined Pole Permanent Magnet Generator for Range-Extended Electric Vehicle

Jiachen An[1], Huihui Geng[1, *], Xia Zhang[2], Deming Kong[1],
Xianshun Wang[2], Jianbo Zhao[1], and Zhiang Liang[1]

[1]*School of Transportation and Vehicle Engineering, Shandong University of Technology, Zibo 255000, China*
[2]*Research and Development Department, Zibo Yongtai Motor Co. Ltd., Zibo 255000, China*

**ABSTRACT:** The interior permanent magnet synchronous generators (IPMSGs) for range-extended electric vehicles (REEVs) have a complex magnetic circuit distribution, which makes it difficult to analyze their electromagnetic characteristics. This paper investigates the electromagnetic characteristics of a combined pole IPMSG topology. An accurate equivalent magnetic circuit model of the generator, taking into account the influence of leakage flux, is established. The magnetic flux equations and precise calculation methods for the main magnetic circuits and leakage magnetic circuits are provided. The accuracy of the equivalent magnetic circuit model is verified using the finite element method. Based on the analysis results, the permanent magnet end of the generator is designed with magnetization isolation. The multi-parameter multi-objective optimization is performed using the particle swarm method to improve the output performance of the generator. A prototype is manufactured and tested. The generator exhibits excellent no-load and load performance, fulfilling the practical requirements and laying a solid foundation for further optimization of the REEV's power system and further improvement of system-level performance.

## 1. INTRODUCTION

With the increasingly serious issues of fossil fuel shortages and environmental pollution, new energy vehicles (NEVs) have become a significant focus for the development of the global automobile industry today [1, 2]. With their unique structural design and energy advantages, range-extended electric vehicles (REEVs) have emerged as a significant segment of NEVs. Compared to electric vehicles (EVs), REEVs are equipped with a range extender (RE) — an auxiliary power generation device consisting of an engine and a generator. The car operates on pure electric drive when the traction battery pack is fully charged. When the traction battery's state of charge falls below the threshold, the engine of the RE activates, driving the generator to produce electric power for the drive motor and traction battery pack. This functionality allows REEVs to not only enjoy the energy-saving and environmentally friendly benefits of EVs but also compensate for the limitations of EVs regarding driving range [3–5].

The generator for RE is one of the core components of REEVs, which must fulfill the main performance requirements of a compact structure and high power generation efficiency simultaneously. Although conventional interior permanent magnet synchronous generators (IPMSGs) (e.g., I-shaped, tangential, and V-shaped) have been widely adopted in NEVs due to their significant advantages in structure and power density compared to other generators [6, 7], the magnetic field at each pole

of their rotors is provided by only one or two permanent magnets (PMs), resulting in relatively low magnetic field strength. In contrast, combined poles incorporating multiple PMs can effectively utilize the rotor core space to provide higher magnetic field strength, reduce the adverse effects of end flux focusing effect of PMs, and better meet the requirements of REs [8].

Magnetic field modeling and electromagnetic analysis of IPMSGs are the basis of their structural design, optimization, and characterization, and have always been the focus of research by many scholars. Currently, the finite element method (FEM) has been widely adopted due to its high computational accuracy; however, it has disadvantages such as time-consuming modeling and a heavy computational load [9, 10]. The analytical method (AM), on the other hand, can obtain electromagnetic parameters without requiring highly accurate modeling or massive computer resources, significantly reducing computation time while providing sufficient analytical accuracy. The two commonly used AMs are the equivalent magnetic circuit method (EMCM) and subdomain method (SM). In terms of modeling and analysis of EMCM, Ref. [11] combined EMCM with the space harmonic method to establish a hybrid equivalent magnetic circuit model of radial I-shaped and V-shaped pole motors, and analyzed the effects of different rotor shapes, no-load induced voltage, and cogging torque on the main air gap magnetic density. Ref. [12] proposed a nonlinear reluctance modeling method combining the rotor potential model with EMCM in their study of interior permanent magnet synchronous motor (IPMSM), which accurately calculates the

rotor surface magnetomotive force distribution, the saturation of magnetic bridge region, and the air gap magnetic field distribution, taking into account the stator-rotor saturation effect. Ref. [13] proposed an EMCM to calculate the analytical model of slotless open-circuit air gap field based on an IPMSM with V-shaped segmented skewing and introduced the relative permeability to obtain the analytical model of the slotted open air gap magnetic field, taking into account the saturation of rotor magnetic bridge and stator slotting effect. Ref. [14] analyzed an IPMSM by using EMCM to construct a magnetic circuit model that can provide the radial component of slotless open-circuit air gap field and obtained an accurate solution for the magnetically dense component in the slotted air gap. Ref. [15] proposed a method for modeling permanent magnet synchronous linear motors based on distributed EMCM. The new model can account for the local magnetic saturation and nonlinear characteristics of the motor.

In terms of modeling and analysis of SM, [16] improved a conventional SM of a surface-mounted permanent magnet synchronous motor (SPMSM) by using boundary discretization method, which divides the magnetic field into three types of subdomains, named stator slot, air gap, and PMs, solves them by using different kinds of equations, and obtains the air gap magnetic density of motor under no load and load conditions. Ref. [17] established an accurate magnetic field model for a single/three-phase dual-port IPMSG, considering stator-rotor magnetic reluctance, based on the analytic method of a nonlinear subdomain model. Ref. [18] proposed a division SM based on the equal-volume chunking treatment of PMs to address the difficulty of analyzing the magnetic field of eccentric segmented pole SPMSM, and the fundamental and harmonic components of the unloaded air gap magnet density were directly obtained by solving the subdomain model. Ref. [19] developed an exact subdomain analytical model for optimizing pole shapes to mitigate the torque ripple of IPMSM after considering the stator slotting effect, PM charging direction, and armature winding layout. Ref. [20] proposed a new method for solving the exact solution of an arbitrary part of the sector subdomain and computationally analyzed the magnetic field of a U-shaped IPMSM after considering the parallel magnetization and saturation of the magnetic bridge.

In summary, EMCM has advantages of simple calculation, intuitive solution, universal application, time-saving, and high efficiency, and has significant advantages in the modeling and analysis of complex topology, but there is a certain lack of solution accuracy; the main magnetic circuit model needs to be further processed to improve the solution accuracy. SM has certain advantages in solution accuracy, but the generator structure limits its application. For generators with complex magnetic poles, selecting the subdomain partitioning strategy and determining the boundary conditions are more challenging; the computational volume of the model increases exponentially, which in turn increases computational time and the difficulty of analysis. Unlike conventional IPMSGs, the rotor of the combined pole IPMSGs contains more magnetic sources and exhibits a more complex magnetic field distribution. Compared to the SM, constructing an accurate equivalent magnetic circuit model is a clearer and more efficient approach. This paper mainly ex-

plores ways to improve the accuracy of the EMCM for complex topologies, focusing on analyzing the leakage magnetic field of PMs and precisely calculating leakage magnetic parameters to create a high-precision model that includes leakage effects. Based on these analyses, parameter optimization is performed on the proposed composite pole rotor to reduce leakage fields and enhance output performance. The validity of the proposed method and the practicality of the new generator are confirmed through FEM and test.
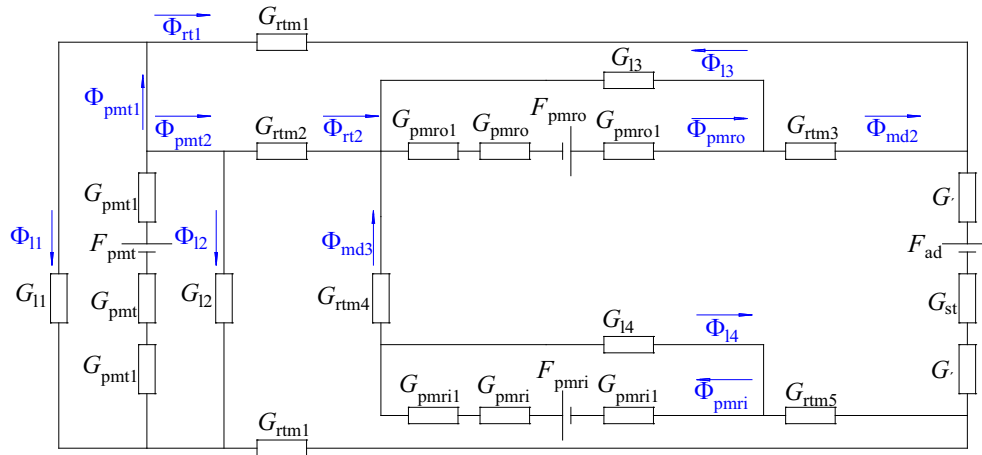
## 2. ELECTROMAGNETIC DESIGN AND ANALYSIS OF THE MAGNETIC CIRCUIT FOR THE COMBINED POLE ROTOR

This paper is based on the conventional IPMSG with tangential permanent magnets (TPMs), adding I-shaped permanent magnets (IPMs) or V-shaped permanent magnets (VPMs) on both sides, resulting in two new types of combined pole IPMSGs. Their structure and magnetic circuit distribution are shown in Figure 1.

From Figure 1(a), the combined pole rotor with IPMs on the inner side and VPMs on the outer side is called the inner and outer V + I-shaped combined pole rotor. There are three main magnetic circuits: magnetic circuit 1 consists of the TPMs acting alone; magnetic circuit 2 includes the TPMs acting with the VPMs; and magnetic circuit 3 involves the IPMs acting with the VPMs. There are five main leakage magnetic circuits: ① and ② represent the leakage circuits at the outer and inner ends of the TPMs; ③ and ④ represent the leakage circuits at the outer and inner ends of the VPMs; and ⑤ denotes the leakage circuit of the IPMs. The equivalent magnetic circuit of the inner and outer V + I-shaped combined pole IPMSG is shown in Figure 2.

From Figure 2, $\Phi_{pmtv1}$ and $\Phi_{pmtv2}$ are the magnetic fluxes of the magnetic circuits where the TPMs are located in the main magnetic circuits 1 and 2. $\Phi_{pmvo}$ is the magnetic flux of the magnetic circuit where VPMs are located in the main magnetic circuit 2. $\Phi_{pmriv}$ is the magnetic flux of the magnetic circuit where IPMs are located in the main magnetic circuit 3. $\Phi_{rtv1}$, $\Phi_{rtv2}$, and $\Phi_{rtv3}$ are the magnetic fluxes through the rotor core in the main magnetic circuits 1, 2, and 3. $\Phi_{mdv2}$ and $\Phi_{mdv3}$ are the effective magnetic fluxes through the main air gap in the main magnetic circuits 2 and 3. $\Phi_{lv1}$, $\Phi_{lv2}$, $\Phi_{lv3}$, $\Phi_{lv4}$, and $\Phi_{lv5}$ are the magnetic fluxes of the five leakage circuits. $G_{pmt}$, $G_{pmvo}$, $G_{pmri}$ are the internal magnetic conductances of TPMs, VPMs, and IPMs. $G_{pmtl}$, $G_{pmvol}$, and $G_{pmril}$ are the magnetic conductances of the gap among the TPMs, VPMs, and IPMs, and the rotor core. $G_{rtm1}$ is the magnetic conductance of the rotor core magnetic circuit between the TPMs and the main air gap in the main magnetic circuits 1 and 2. $G_{rtm2}$ and $G_{rtm3}$ are the magnetic conductance of the rotor core magnetic circuit between the TPMs and VPMs in the main magnetic circuit 2 as well as between the VPMs and the main air gap. $G_{rtm4}$ and $G_{rtm5}$ are the magnetic conductance of the rotor core magnetic circuit between the VPMs and IPMs in the main magnetic circuit 3, and between the IPMs and the main air gap. $G_{l1}$, $G_{l2}$, $G_{l3}$, $G_{l4}$, and $G_{l5}$ are the magnetic conductance of the five leakage circuits. $G_{st}$ and $G_{\delta}$ are the magnetic conductance of the stator core and

**FIGURE 1**. Structure and magnetic circuit distribution of different combined-pole IPMSGs.



**FIGURE 2**. Equivalent magnetic circuit of the inner and outer V + I-shaped combined pole IPMSG.

the main air gap. $F_{pmt}$, $F_{pmvo}$, and $F_{pmri}$ are the magnetomotive force generated by TPMs, VPMs, and IPMs. $F_{ad}$ is the direct-axis armature reaction magnetomotive force. $F_{ad} = 0$ under no-load condition.

The equivalent magnetic circuit models of the three main magnetic circuits of the inner and outer V + I-shaped combined pole IPMSG are established, and the flux equation systems are as follows [21–23]:

$$\begin{cases} \Phi_{pmtv1} = \Phi_{rtv1} + \Phi_{lv1} \\ F_{pmt} = \Phi_{pmtv1}\left(\frac{1}{G_{pmt}} + \frac{2}{G_{pmtl}}\right) + \frac{\Phi_{lv1}}{G_{l1}} \\ 2\Phi_{rtv1}\left(\frac{1}{G_{rtm1}} + \frac{1}{G_{\delta}}\right) + \frac{\Phi_{rtv1}}{G_{st}} - \frac{\Phi_{lv1}}{G_{l1}} - F_{ad} = 0 \end{cases} \quad (1)$$

$$\begin{cases} \Phi_{pmtv2} = \Phi_{lv2} + \Phi_{rtv2} \\ \Phi_{rtv2} = \Phi_{lv3} + \Phi_{pmvo} \\ \Phi_{pmvo} + \Phi_{lv3} = \Phi_{mdv2} \\ F_{pmt} + \Phi_{pmtv2}\left(\frac{1}{G_{pmt}} + \frac{2}{G_{pmtl}}\right) - \frac{\Phi_{lv2}}{G_{l2}} = 0 \\ F_{pmvo} + \Phi_{pmvo}\left(\frac{1}{G_{pmvo}} + \frac{2}{G_{pmvol}}\right) + \frac{\Phi_{lv3}}{G_{l3}} = 0 \\ \frac{\Phi_{rtv2}}{G_{rtm2}} - \frac{\Phi_{l3}}{G_{l3}} - \Phi_{mdv2}\left(\frac{2}{G_{\delta}} + \frac{1}{G_{st}} + \frac{1}{G_{rtm1}} + \frac{1}{G_{rtm3}}\right) \\ + \frac{\Phi_{lv2}}{G_{l2}} + F_{ad} = 0 \end{cases} \quad (2)$$

$$\begin{cases} \Phi_{pmriv} = \Phi_{lv5} + \Phi_{rtv3} \\ \Phi_{rtv3} = \Phi_{lv4} + \Phi_{pmvo} \\ \Phi_{pmvo} + \Phi_{lv4} = \Phi_{mdv3} \\ F_{pmri} = \Phi_{pmriv}\left(\frac{1}{G_{pmri}} + \frac{2}{G_{pmril}}\right) + \frac{\Phi_{lv5}}{G_{l5}} \\ F_{pmvo} + \Phi_{pmvo}\left(\frac{1}{G_{pmvo}} + \frac{2}{G_{pmvol}}\right) + \frac{\Phi_{lv4}}{G_{l4}} = 0 \\ \frac{\Phi_{rtv3}}{G_{rtm4}} - \frac{\Phi_{lv4}}{G_{l4}} - \Phi_{mdv3}\left(\frac{2}{G_{\delta}} + \frac{1}{G_{st}} + \frac{1}{G_{rtm3}} + \frac{1}{G_{rtm5}}\right) \\ + \frac{\Phi_{lv5}}{G_{l5}} + F_{ad} = 0 \end{cases} \quad (3)$$

From Figure 1(b), the combined pole rotor with both inner and outer IPMs is called the inner and outer I-shaped combined pole rotor. There are three main magnetic circuits: magnetic circuit 1 is the TPMs acting alone; magnetic circuit 2 is the TPMs and outer IPMs acting together; and magnetic circuit 3 is the inner and outer IPMs acting together. There are four main leakage circuits: ① and ② are the end leakage circuits of the outer and inner ends of TPMs; ③ is the end leakage circuit of the outer IPMs; and ④ is the end leakage circuit of the inner IPMs. The equivalent magnetic circuit of the inner and outer I-shaped combined pole IPMSG is shown in Figure 3.

From Figure 3, $\Phi_{pmt1}$ and $\Phi_{pmt2}$ are the magnetic fluxes of the magnetic circuits where the TPMs are located in the main

**FIGURE 3**. Equivalent magnetic circuit of the inner and outer I-shaped combined pole IPMSG.

magnetic circuits 1 and 2. $\Phi_{pmro}$ is the magnetic flux of the magnetic circuit where the outer IPMs are located in the main magnetic circuit 2. $\Phi_{pmri}$ is the magnetic flux of the magnetic circuit where the inner IPMs are located in the main magnetic circuit 3. $\Phi_{rt1}$ and $\Phi_{rt2}$ are the magnetic fluxes through the rotor core in the main magnetic circuits 1 and 2. $\Phi_{md2}$ and $\Phi_{md3}$ are the effective magnetic fluxes through the main air gap in the main magnetic circuits 2 and 3. $\Phi_{l1}$, $\Phi_{l2}$, $\Phi_{l3}$, and $\Phi_{l4}$ are the magnetic fluxes of the four leakage circuits. $G_{pmro}$ is the internal magnetic conductance of the outer IPMs. $G_{pmrol}$ is the magnetic conductance of the gap between the outer IPMs and the rotor core. $G_{rtm2}$ and $G_{rtm3}$ are the magnetic conductance of the rotor core magnetic circuit between the TPMs and outer IPMs in the main magnetic circuit 2, as well as between the outer IPMs and the main air gap. $G_{rtm4}$ and $G_{rtm5}$ are the magnetic conductance of the rotor core magnetic circuit between the inner and outer IPMs in the main magnetic circuit 3, and between the inner IPMs and the main air gap. $F_{pmro}$ is the magnetomotive force generated by the outer IPMs.

The equivalent magnetic circuit models of the three main magnetic circuits of the inner and outer I-shaped combined pole IPMSG are established, and the flux equation systems are as follows:

$$
\begin{cases}
\Phi_{pmt1} = \Phi_{rt1} + \Phi_{l1} \\
F_{pmt} = \Phi_{pmt1}\left(\frac{1}{G_{pmt}} + \frac{2}{G_{pmtl}}\right) + \frac{\Phi_{l1}}{G_{l1}} \\
2\Phi_{tr1}\left(\frac{1}{G_{rtm1}} + \frac{1}{G_\delta}\right) + \frac{\Phi_{rt1}}{G_{st}} - \frac{\Phi_{l1}}{G_{l1}} - F_{ad} = 0
\end{cases} \quad (4)
$$

$$
\begin{cases}
\Phi_{pmt2} = \Phi_{l2} + \Phi_{rt2} \\
\Phi_{rt2} = \Phi_{l3} + \Phi_{pmro} \\
\Phi_{pmro} + \Phi_{l3} = \Phi_{md2} \\
F_{pmt} + \Phi_{pmt2}\left(\frac{1}{G_{pmt}} + \frac{2}{G_{pmtl}}\right) - \frac{\Phi_{l2}}{G_{l2}} = 0 \\
F_{pmvo} + \Phi_{pmro}\left(\frac{1}{G_{pmro}} + \frac{2}{G_{pmrol}}\right) + \frac{\Phi_{l3}}{G_{l3}} = 0 \\
\frac{\Phi_{rt2}}{G_{rtm2}} - \frac{\Phi_{l3}}{G_{l3}} - \Phi_{md2}\left(\frac{2}{G_\delta} + \frac{1}{G_{st}} + \frac{1}{G_{rtm1}} + \frac{1}{G_{rtm3}}\right) \\
+ \frac{\Phi_{l2}}{G_{l2}} + F_{ad} = 0
\end{cases} \quad (5)
$$

$$
\begin{cases}
\Phi_{pmri} = \Phi_{l4} + \Phi_{md3} \\
F_{pmri} = \Phi_{pmri}\left(\frac{1}{G_{pmri}} + \frac{2}{G_{pmril}}\right) + \frac{\Phi_{l4}}{G_{l4}} \\
F_{pmro} = \Phi_{md3}\left(\frac{1}{G_{pmro}} + \frac{2}{G_{pmrol}} + \frac{2}{G_\delta} + \frac{1}{G_{st}}\right. \\
\left. + \frac{1}{G_{rtm3}} + \frac{1}{G_{rtm5}} + \frac{1}{G_{rtm4}}\right) + F_{ad} - \frac{\Phi_{l4}}{G_{l4}}
\end{cases} \quad (6)
$$

The computational parameters in the system of flux equations can be calculated according to the following equations, respectively [24, 25]:

### 2.1. Magnetic Conductance of the Main Air Gap

The magnetic conductance of the main air gap $G_\delta$ is calculated as:

$$
G_\delta = \frac{\mu_0 \pi \left(D_{i1} + D_{r1}\right) L_{st}}{4 p_r \delta} \quad (7)
$$

where $D_{i1}$ is the stator bore diameter, $D_{r1}$ the rotor outer diameter, $\mu_0$ the vacuum permeability, $p_r$ the number of rotor pole pairs, $L_{st}$ the stator core axial length, and $\delta$ the main air gap length.

### 2.2. Magnetic Conductance of the Stator Core

The magnetic conductance of the stator core $G_{st}$ is calculated as:

$$
G_{st} = \frac{G_{stA} G_{stB}}{G_{stA} + G_{stB}} \quad (8)
$$

where $G_{stA}$ is the magnetic conductance of the stator tooth, and $G_{stB}$ is the magnetic conductance of the stator yoke.

The stator tooth can be approximately divided into $k$ trapezoidal regions along the radial direction, and $G_{stA}$ can be calculated as:

$$
G_{stA} = \frac{1}{\sum \frac{h_{t(k+1)}}{\mu_{rt0}\mu_0\pi\left[b_{tk}+b_{t(k+1)}\right]L_{st}}} \quad (9)
$$

where $\mu_{rt0}$ is the relative permeability of the silicon steel lamination core, which is taken as 8000, $b_{tk}$ the width of the lower

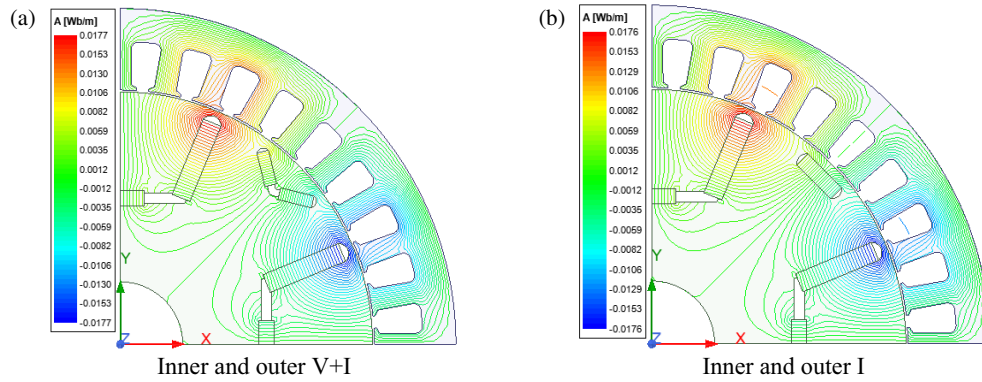(a) Inner and outer V+I

(b) Inner and outer I

FIGURE 4. Magnetic flux distribution of two combined pole IPMSGs.

and upper bases of the trapezoid in which each part is located, and $h_{t(k+1)}$ the height of the trapezoid in which each part is located.

The circumferential length of the stator yoke varies with different positions of the rotor magnetic circuit, and the longest magnetic circuit is selected for the calculation of the permeability:

$$G_{stB} = \frac{2\mu_{rt0}\mu_0 h_j L_{st} p_r}{\pi (D_{st1} - h_j)} \quad (10)$$

where $h_j$ is the height of the stator yoke, and $D_{st1}$ is the stator outer diameter.

## 2.3. Associated Conductance of the PMs

The internal magnetic conductance $G_{pm}$ and the magnetic conductance of the gap between each PM and the rotor core $G_{pm1}$ of each PM can be calculated as:

$$G_{pm(1)} = \frac{\mu_{pm0}\mu_0 a_{pm} L_{rt}}{h_{pm(1)}} \quad (11)$$

where $\mu_{pm0}$ is the relative permeability of the PMs (1.05 for PMs and 1 for air), $L_{rt}$ the axial length of the rotor, $a_{pm}$ the length of each PM, $h_{pm}$ the magnetization direction length of PMs, and $h_{pm1}$ the length of the gap between the length direction of each PM and the rotor core.

## 2.4. Magnetic Conductance of the Rotor Core

$G_{rtm1}$, $G_{rtm3}$, and $G_{rtm5}$ are the conductance of the magnetic circuit of the rotor core between the PMs and the main air gap, calculated as:

$$G_{rtm} = \frac{\mu_{rt0}\mu_0 a_{rm} L_{rt}}{l_{rm}} \quad (12)$$

where $a_{rm}$ is the length of the part of the magnetic field provided by each PM individually in the magnetic circuit, and $l_{rm}$ is the length of the rotor core magnetic circuit between each PM and the main air gap.

$G_{rtm2}$ and $G_{rtm4}$ are the conductance of the magnetic circuit of the rotor core between the two PMs, calculated as:

$$G_{rtm} = \frac{\mu_{rt0}\mu_0 (a_{pm} - a_{rm}) L_{rt}}{l_{rtm}} \quad (13)$$

where $l_{rtm}$ is the length of the magnetic circuit of the rotor core between the two PMs.

The leakage circuit at the end of each PM can be simplified to a circular arc of radius $r_{lo}$, calculated as:

$$r_{lo} = \frac{(h_{pm} + 2h_{el})^2 + 4(a_{et} + a_{el})^2}{8(a_{et} + a_{el})} \quad (14)$$

where $h_{el}$ is the length of a straight line in the direction of the thickness of each PM, $a_{et}$ the perpendicular distance from the center of the arc to each PM, and $a_{el}$ the distance between the straight line portion and the outer end of each PM.

The magnetic conductance of the leakage magnetic circuit $G_l$ can be calculated as:

$$G_l = \frac{\mu_{rt0}\mu_0 L_{rt} a_{et}}{r_{lo}\arcsin((h_{pm} + 2h_{el})/2r_{lo})} \quad (15)$$

The magnetic flux, leakage flux, and leakage coefficient of each magnetic circuit can be obtained by solving the system of flux equations, which involves calculating magnetic dynamic potential, magnetic conduction, and leakage conduction. Additionally, to verify the validity of these calculation results, two types of combined pole IPMSG finite element models are established and simulated. The distribution of magnetic flux for the two IPMSGs is shown in Figure 4.

From Figure 4, the FEM results align with the primary magnetic circuit and leakage circuit distribution derived from the magnetic circuit analysis of the EMCM. However, the FEM rotor magnetic circuit is nearly elliptical, and the ends of the PMs show an increased amount of magnetic leakage. The magnetic fluxes at various pole positions for the two rotors are calculated separately using finite element software and compared with the results obtained from the EMCM, as shown in Table 1.

From Table 1, the rotor flux per pole calculated by the FEM is slightly lower than that calculated by the EMCM, with the total difference in rotor flux between the two methods being approximately $3 \times 10^{-5}$ Wb. However, the results obtained by the two methods differ only slightly. Considering that the EMCM can effectively save computation time compared to the FEM, a comprehensive analysis shows that the accurate EMCM proposed in this paper performs well when solving the electromagnetic characteristics of the combined pole IPMSG. A comparison of the analysis results for the two rotors shows that the

**TABLE 1**. Results of FEM and EMCM calculations of magnetic flux of two combined pole IPMSGs.

| Structure | Flux at pole center /Wb | | Flux at pole edge /Wb | | | | | Total flux /Wb | |
|---|---|---|---|---|---|---|---|---|---|
| | EMCM | | EMCM | | | | | EMCM | FEM |
| | Main magnetic circuit 1 | FEM | Main magnetic circuit 2 | Main magnetic circuit 3 | Total | FEM | | | |
| Inner and outer V + I | $1.225 \times 10^{-4}$ | $1.229 \times 10^{-4}$ | $8.464 \times 10^{-5}$ | $8.120 \times 10^{-5}$ | $1.658 \times 10^{-4}$ | $1.502 \times 10^{-4}$ | | $5.767 \times 10^{-4}$ | $5.454 \times 10^{-4}$ |
| Inner and outer I | $1.631 \times 10^{-4}$ | $8.396 \times 10^{-5}$ | $4.390 \times 10^{-5}$ | $8.671 \times 10^{-5}$ | $1.306 \times 10^{-4}$ | $1.945 \times 10^{-4}$ | | $5.874 \times 10^{-4}$ | $5.570 \times 10^{-4}$ |
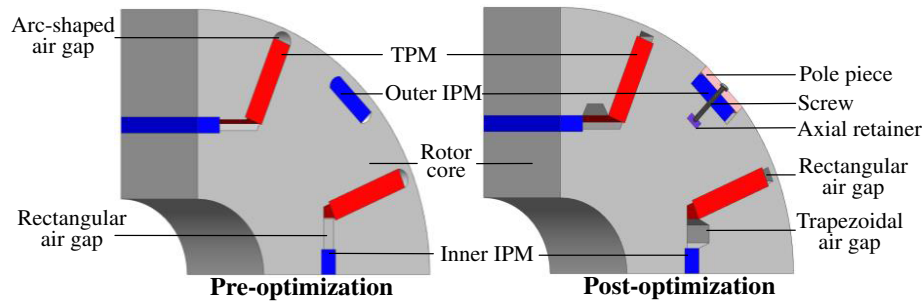


**FIGURE 5**. Optimization of the structure of the inner and outer I-shaped combined pole rotor.

magnetic field produced by the TPM in magnetic circuit 1 of the two combined pole rotors directly enters the main air gap through the rotor core. The other two magnetic circuits are in series with two PMs to supply the magnetic field, and their reluctance is relatively high, resulting in lower fluxes in magnetic circuits 2 and 3 than magnetic circuit 1. Nevertheless, the magnetic flux at the center of the magnetic poles increases due to the combined PM effect. In the inner and outer V + I-shaped combined pole rotor, the presence of more VPMs and TPMs in series leads to a relatively larger magnetic flux in magnetic circuit 2. Furthermore, because the calculation range for the magnetic field at the center of the poles is expanded, the total magnetic flux from magnetic circuits 2 and 3 increases. However, the flux provided solely by the TPM decreases, making the total flux from this type of combined pole rotor smaller than that from the inner and outer I-shaped combined pole rotor. Consequently, this paper adopts the structure of the inner and outer I-shaped combined pole rotor.

## 3. STRUCTURE AND OUTPUT PERFORMANCE OPTIMIZATION OF THE COMBINED POLE IPMSG

Based on the results of the EMCM analysis above, the magnetic isolation design of the combined pole rotor is conducted. To increase the magnetic reluctance of the leakage circuit ①, the arc-shaped air gap tangential to the outside of the PM is modified into a rectangle. To enhance the magnetic reluctance of leakage circuits ② and ④ simultaneously, the connecting air gaps tangential to the inner side of the PM and the end of the inner IPM are altered to a trapezoidal shape. To boost the magnetic reluctance of the leakage circuit ③, the outer IPM is changed from a

built-in type to an internally buried surface-mounted type. The structure optimization of the inner and outer I-shaped combined pole rotor is shown in Figure 5, both pre-optimization and post-optimization

The output power of the generator can be calculated as [26–28]:

$$P_{\mathrm{pmN}} = \frac{f K_{\mathrm{u}} K_{\mathrm{B}} C \left(BH\right)_{\max} V_{\mathrm{pm}}}{255 \sigma_0 K_{\mathrm{ad}}} \quad (16)$$

where $P_{\mathrm{pmN}}$ is the design power of the generator, $f$ the frequency of the generator, $C$ the maximum magnetic energy utilization factor, $(BH)_{\max}$ the maximum energy product of the PM, $V_{\mathrm{pm}}$ the volume of the PM, $\sigma_0$ the no-load leakage coefficient of the PM field, and $K_{\mathrm{u}}$ the voltage waveform coefficient, calculated as:

$$K_{\mathrm{u}} = \frac{\left[\sqrt{1 - \left(U_{\mathrm{N}} \cos \varphi / E_0\right)^2} - U_{\mathrm{N}} \sin \varphi / E_0\right] U_{\mathrm{N}}}{E_0} \quad (17)$$

where $U_{\mathrm{N}}$ is the rated phase voltage of the generator, $E_0$ the no-load induced voltage of the generator, $K_{\mathrm{B}}$ the power factor. $K_{\mathrm{ad}}$ is the direct-axis armature reaction magnetomotive force reduction factor, calculated as:

$$K_{\mathrm{ad}} = \frac{\alpha_{\mathrm{r}} \pi + \sin \alpha_{\mathrm{r}} \pi}{4 \sin \left(\alpha_{\mathrm{r}} \pi / 2\right)} \quad (18)$$

where $\alpha_{\mathrm{r}}$ is the pole arc coefficient.

From the above equations, the output performance of the generator is mainly related to the material and length of the PM,
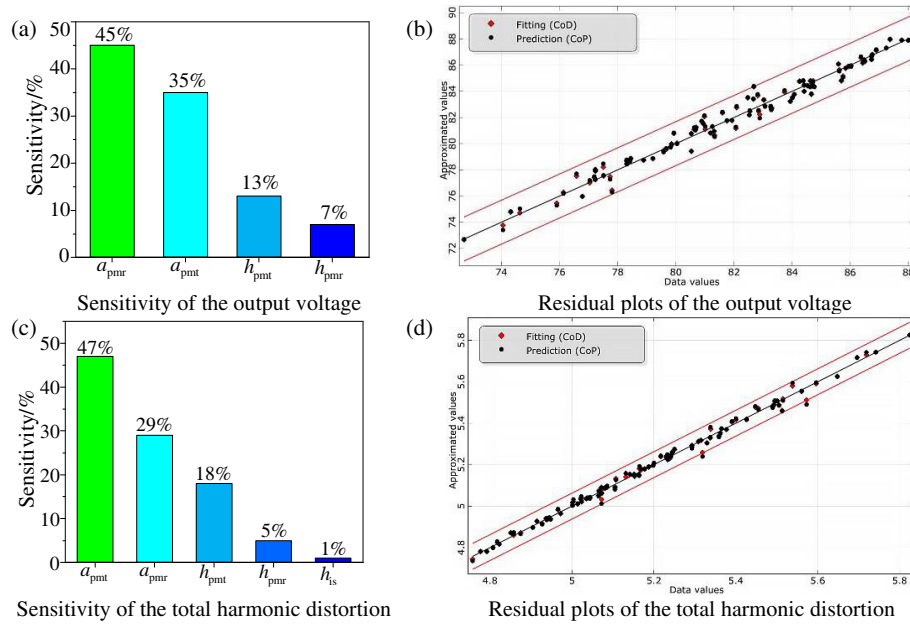
**FIGURE 6**. Sensitivity and residual plots of each design variable to the target parameters.

the length of the magnetizing direction, the position, and other dimensional parameters. To improve the generator output performance, the multi-parameter multi-objective optimization of the PM is carried out using the multi-objective particle swarm optimization. The particle swarm method (PSM) has few adjustment parameters and fast convergence speed, which is suitable for analyzing the influence of PM parameters on the output performance of IPMSGs [29, 30].

The PSM is used to set up an $n$-dimensional space with a particle matrix consisting of $m$ particles, i.e., $x = (x_1, x_2, \ldots, x_m)^{\mathrm{T}}$, where the position and velocity of the $i$th particle are $x_i = (x_{i,1}, x_{i,2}, \ldots, x_{i,n})^{\mathrm{T}}$ and $v_i = (v_{i,1}, v_{i,2}, \ldots, v_{i,n})^{\mathrm{T}}$. The local optimum in the particle matrix is $p_{ib} = (p_{i,1}, p_{i,2}, \ldots, p_{i,n})^{\mathrm{T}}$, and the global optimum of the particle swarm in the optimization process is $g_{ib} = (g_{i,1}, g_{i,2}, \ldots, g_{i,n})^{\mathrm{T}}$. At the end of the iteration, the output of the program is the optimal solution of the PSM.

To obtain the global optimal solution quickly, the particle update position and velocity algorithm is set as:

$$\begin{cases} v_{i,d+1} = \omega_l v_{i,d} + c_1 r_{g1}\left(p_{i,d} - x_{i,d}\right) + c_2 r_{g2}\left(g_{i,d} - x_{i,d}\right) \\ x_{i,d+1} = x_{i,d} + v_{i,d+1} \end{cases} \quad (19)$$

where $\omega_l$ is the inertia factor; $c_1$ and $c_2$ are the acceleration factors, where $c_1$ is the ability of an individual particle to push to a local extreme, and $c_2$ is the ability of an individual particle to push to a global extreme; $r_{g1}$ and $r_{g2}$ are two random numbers independent of each other in the interval $(0, 1)$.

The length of each PM, the length of the magnetizing direction, and the distance from the outer end of each PM to the outer circle of the rotor are selected as the analysis variables. The optimization objective is set to minimize the load output voltage and the no-load total harmonic distortion within the constraint range of variables. The simulation analysis is conducted on 100 sampling points, each with six design variables, and the sensi-

tivity and residual plots for each design variable to the target parameters are presented in Figure 6.

From Figures 6(a) and 6(c), the design variable distributions of the PM length show higher sensitivity to the rated load output voltage and the no-load total harmonic distortion. Among them, the combined PM length exhibits the highest sensitivity of 45% to the rated load output voltage, while the TPM length demonstrates the highest sensitivity of 47% to the no-load total harmonic distortion. From Figures 6(b) and 6(d), the output data from each sample point fit well, with most data points clustered around the fitting line, indicating a linear relationship with the optimization target parameters.

To further determine the optimal parameters, the results are analyzed using the Pareto optimization method. 100 sample points were analyzed, and the Pareto front distribution is shown in Figure 7.

From Figure 7, a total of 27 optimal values are obtained using the Pareto method, and the sample points of maximum load condition output voltage and minimum no-load total harmonic distortion are selected as the optimal solution of the optimization algorithm. However, the optimal parameters are the opti-
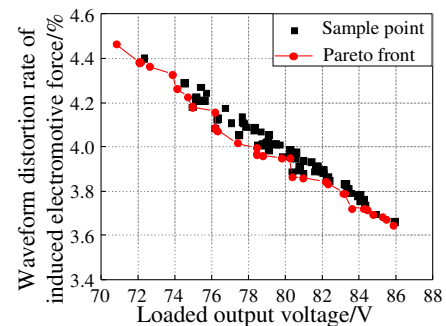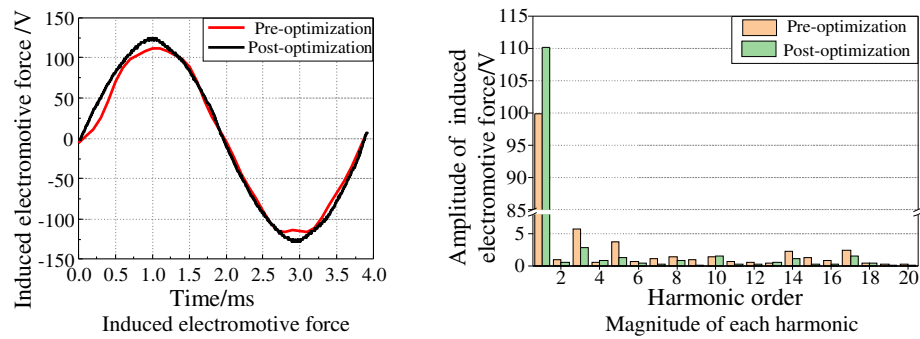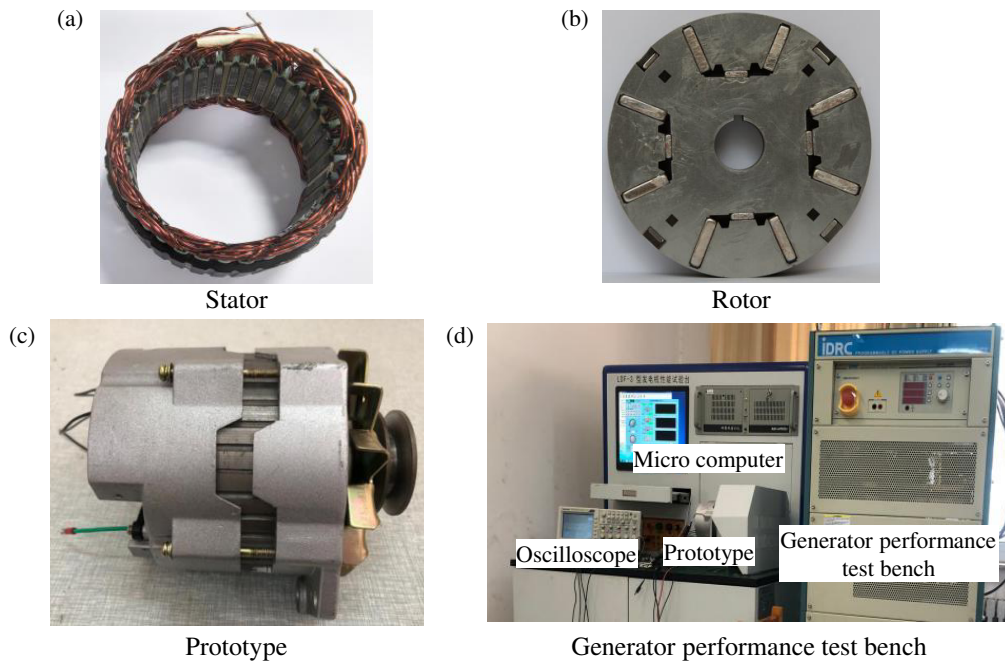


**FIGURE 7**. Pareto front distribution.

**FIGURE 8**. Induced electromotive force waveform and amplitude of each harmonic.



(a) Stator  (b) Rotor  (c) Prototype  (d) Generator performance test bench

**FIGURE 9**. Prototype structure and generator performance test bench.

**TABLE 2**. Constraint ranges of PM parameters and values.

| Design variable (mm) | Constraint range | Initial value | Optimal value | Final value |
|---|---|---|---|---|
| Length of the TPM | 14–16 | 15 | 14.844 | 15 |
| Length of the TPM magnetization direction | 4–5.5 | 4 | 4.4825 | 4.5 |
| Distance from the TPM to the rotor outer circle | 1–3 | 2 | 1.77 | 1.8 |
| Length of the combined PM magnetization direction | 2–3.5 | 2.5 | 2.795 | 3 |
| Length of combined PM | 11–13 | 10 | 11.395 | 12 |
| Distance from the combined PM to the rotor outer circle | 1.5–3.5 | 2 | 1.65 | 1.7 |

mal values of the ideal state, and the optimal values need to be modified considering the actual processing problems. The constraint ranges, initial values, optimal values, and final values of the PM parameters are shown in Table 2.

Using the optimized parameters to conduct the analysis, the optimized no-load induced electromotive force waveform and the induced electromotive force amplitude of each harmonic are obtained, as shown in Figure 8.

From Figure 8(a), both the peak and smoothness of the waveform of the induced electromotive force improve after optimization. From Figure 8(b), after optimization, the fundamental amplitude of the induced electromotive force increases, while the amplitude of each harmonic decreases. Specifically, the amplitude of the 3rd harmonic drops from 5.72 V to 2.82 V, marking a decrease of 50.70%, while the 5th harmonic falls from 3.63 V to 1.34 V, a decrease of 63.09%. The total har-
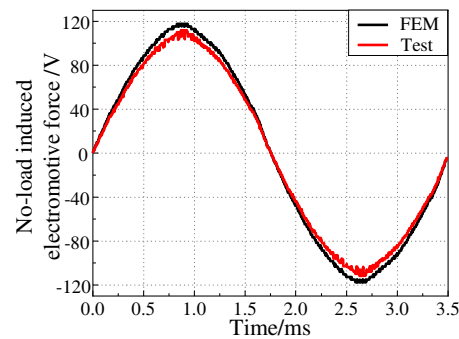
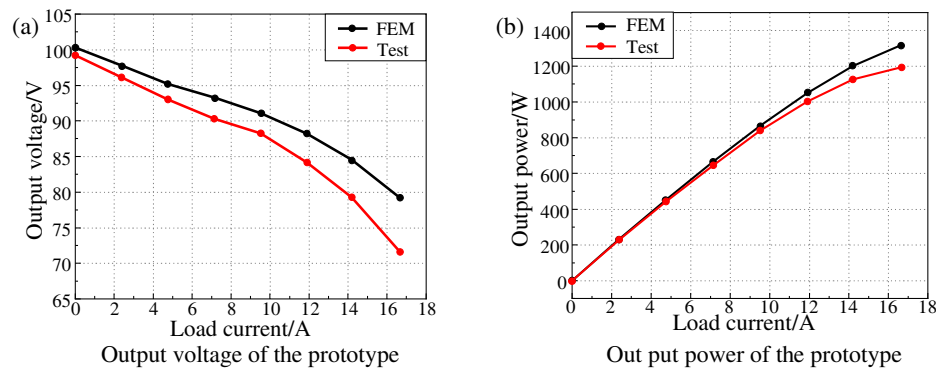**FIGURE 10**. No-load induced electromotive force of the prototype.



**FIGURE 11**. External characteristic curve of the prototype.

**TABLE 3**. Main performance indexes and structural parameters of the prototype.

| Parameter | Value | Parameter | Value |
|---|---|---|---|
| Rated voltage/V | 84 | Outer diameter of the stator/mm | 140 |
| Rated power/W | 1000 | Inner diameter of the stator/mm | 106 |
| Rated speed/rpm | 4000 | Inner diameter of the rotor/mm | 26 |
| PM material | N38H | Length of the main air gap/mm | 0.4 |
| Stator and rotor core material | DW310-35 | Axial length of the IPMSG/mm | 27 |

monic distortion is calculated at 4.37% pre-optimization and 3.64% post-optimization, representing a reduction of 16.70%. The output voltages under rated load conditions are 84.35 V and 86.21 V, respectively. After optimization, the output voltage increases by 1.86 V. The optimized parameters of the PMs effectively enhance the generator's output voltage, reduce the induced electromotive force harmonics, and subsequently improve its output characteristics.

## 4. PROTOTYPING AND TESTING

A prototype of the combined pole IPMSG is fabricated based on the optimized PM parameters with reference to the design specifications of IPMSGs. The main performance indexes and other main parameters of the prototype are shown in Table 3. A generator test bench was used to test its performance. The prototype structure and generator performance test bench are shown in Figure 9.

The generator speed is set to the rated value, and no winding is connected at the armature end to test the no-load induced electromotive force of the prototype. Compare it with the FEM. The no-load induced electromotive force waveform of the prototype is shown in Figure 10.

From Figure 10, the FEM results of the no-load induced electromotive force waveform of the prototype are the same as the test results in the same period. The output no-load induced electromotive force waveform has high smoothness, which is only slightly smaller than that of the FEM results at the wave peak, and there are fewer aberrations in the middle of the waveform, which indicates that there are fewer harmonics in the main magnetic field of the generator after the optimization of the structure, and the prototype has a high output performance.

Setting the prototype speed to the rated speed, changing the size of the load resistance, testing its output voltage and power, and comparing it with the FEM results, the output voltage and power of the prototype are shown in Figure 11.

From Figure 11, the output voltage of the prototype decreases as the load current increases. Since this paper uses purely resistive loads for simulation, there is a degree of error in the testing process; the output voltage test results under different loads are slightly lower than the FEM results. As the load current increases, the discrepancy between the two grows, but the overall error remains small. At the rated load current of 11.9 A, the output voltage reaches 84.16 V, which meets the design requirements of the generator. As the load current increases, the output power of the prototype gradually rises. The output power test results under varying load currents are slightly lower than the FEM results, but the difference is minimal. When the load current is increased to 11.9 A, the output power of the test prototype is 1001.50 W, which satisfies the design requirements.

## 5. CONCLUSIONS

This paper adopts the EMCM to analyze the electromagnetic characteristics and select the optimal design for the proposed different combined pole IPMSG. Establish a complex equivalent magnetic circuit model while considering the influence of leakage magnetism, obtain the analytical solutions for flux and leakage flux in the magnetic circuit model, and compare them with the results from the FEM to verify the accuracy of the EMCM and the effectiveness of the method proposed in this paper. Based on the results, the magnetic isolation is designed for the major leakage flux. With the maximum rated load output voltage and minimum no-load induced electromotive force waveform distortion rate as the optimization objectives, a multi-objective particle swarm algorithm is used to optimize the PM parameters. After optimization, the no-load induced electric potential of the generator enhances the smoothness of wave peaks and waveforms, reduces the amplitude of all harmonics, and significantly increases the output voltage under the rated load condition. A prototype is fabricated and tested, showing that the generator achieves good no-load and load output performances. This paper provides an important design basis and reference for further constructing an efficient power generation model for REEVs, improving the compactness and light weight of the power system, and increasing the working efficiency of the entire vehicle.

## REFERENCES

[1] Pata, S. K., S. Erdogan, U. K. Pata, and M. S. Meo, "Greening road transport: Comparison of technologies in conventional, hybrid, and electric vehicles," *Journal of Environmental Management*, Vol. 380, 124908, 2025.

[2] Liu, X., J. Guo, R. Lu, Z. Liu, and B. Sun, "Design and analysis of a delta-shaped segmented variable leakage flux reverse-salient permanent magnet synchronous machine for electric vehicles," *Progress In Electromagnetics Research C*, Vol. 152, 197–208, 2025.

[3] Tran, M.-K., A. Bhatti, R. Vrolyk, D. Wong, S. Panchal, M. Fowler, and R. Fraser, "A review of range extenders in battery electric vehicles: Current progress and future perspectives," *World Electric Vehicle Journal*, Vol. 12, No. 2, 54, 2021.

[4] Lan, S., R. Stobart, and R. Chen, "Performance comparison of a thermoelectric generator applied in conventional vehicles and extended-range electric vehicles," *Energy Conversion and Management*, Vol. 266, 115791, 2022.

[5] Rajan, P. S., M. A. Prasanna, M. N. Ahamed, and R. Sathishkumar, "Enhancing the performance and economic efficiency of range-extended electric vehicles: A hybrid dual stream spectrum deconvolution neural network with Beluga Whale Optimization," *Journal of Energy Storage*, Vol. 104, 114450, 2024.

[6] Gao, M., Z. Yu, W. Jiao, W. Hu, H. Geng, Y. Liu, S. Liu, and Y. Liu, "Study on electromagnetic performance of permanent magnet rotor and dual stator starter generator for electric vehicle range extender," *Progress In Electromagnetics Research B*, Vol. 106, 39–55, 2024.

[7] Xiao, D., L. Shi, F. Li, S. Gao, and X. Tao, "Electromagnetic characteristics study of segmental rotor dual mode reluctance starter generator," *IEEE Transactions on Transportation Electrification*, Vol. 11, No. 1, 204–214, 2025.

[8] Shabanpour, M., F. Farrokh, V. Z. Faradonbeh, A. Vahedi, and P. Asef, "Design and hybrid analytical model for interior permanent magnet generator in an electric vehicle auxiliary power unit application," *IET Electrical Systems in Transportation*, Vol. 2025, No. 1, 6472337, 2025.

[9] Saneie, H. and Z. Nasiri-Gheidari, "Performance analysis of outer-rotor single-phase induction motor based on magnetic equivalent circuit," *IEEE Transactions on Industrial Electronics*, Vol. 68, No. 2, 1046–1054, 2021.

[10] Jalali, E., A. Rahideh, and M. H. Javanmardi, "Two-dimensional analytical modeling for slotless spoke type permanent magnet synchronous machines considering ferromagnetic parts permeability," *IEEE Transactions on Magnetics*, Vol. 60, No. 8, 1–10, 2024.

[11] Song, I.-S., B.-W. Jo, and K.-C. Kim, "Analysis of an IPMSM hybrid magnetic equivalent circuit," *Energies*, Vol. 14, No. 16, 5011, 2021.

[12] Wu, S., T. Shi, L. Guo, H. Wang, and C. Xia, "Accurate analytical method for magnetic field calculation of interior PM motors," *IEEE Transactions on Energy Conversion*, Vol. 36, No. 1, 325–337, 2021.

[13] An, Y., C. Ma, N. Zhang, Y. Guo, M. Degano, C. Gerada, Q. Li, and S. Zhou, "Open-circuit air-gap magnetic field calculation of interior permanent magnet synchronous motor with V-shaped segmented skewed poles using hybrid analytical method," *IEEE Transactions on Magnetics*, Vol. 57, No. 12, 1–9, 2021.

[14] Ma, C., J. Zhang, J. Wang, N. Yang, Q. Liu, S. Zuo, X. Wu, P. Wang, J. Li, and J. Fang, "Analytical model of open-circuit air-gap field distribution in interior permanent magnet machines based on magnetic equivalent circuit method and boundary conditions of macroscopic equations," *IEEE Transactions on Magnetics*, Vol. 57, No. 3, 1–9, 2021.

[15] Krämer, C., A. Kugi, and W. Kemmetmüller, "Modeling of a permanent magnet linear synchronous motor using magnetic equivalent circuits," *Mechatronics*, Vol. 76, 102558, 2021.

[16] Dong, L., W. Li, and Z. Shuai, "An improved subdomain model for predicting the magnetic field of a motor containing non-orthogonal boundaries," *IEEE Transactions on Energy Conversion*, Vol. 37, No. 3, 2048–2057, 2022.

[17] Li, K., B. Zhang, G. Feng, and K. Liu, "No-load characteristic analysis of single/three-phase dual-port permanent magnet synchronous generator with eccentric magnetic metal block based on nonlinear magnetic field analytical method," *IEEE Access*, Vol. 11, 132 955–132 965, 2023.

[18] Zhang, J., J. Hu, G. Gu, and F. Du, "Analytical calculation of air gap magnetic field of SPMSM with eccentrically cut poles based on magnetic pole division," *Energies*, Vol. 16, No. 11, 4450, 2023.

[19] Jabbari, A., "An analytical study on iron pole shape optimization in high-speed interior permanent magnet machines," *Iranian Journal of Science and Technology, Transactions of Electrical Engineering*, Vol. 44, No. 1, 169–174, 2020.

[20] Zhou, H., X. Wang, W. Zhao, Z. Xing, and X. Li, "Magnetic field calculation of the U-shaped interior permanent-magnet synchronous machine considering the parallel magnetization and bridge saturation," *IEEE Transactions on Industrial Electronics*, Vol. 71, No. 10, 11 817–11 828, 2024.

[21] Huang, R., Z. Song, Z. Dong, and C. Liu, "An improved magnetic equivalent circuit method for segmented-halbach axial-flux permanent magnet machines," *IEEE Transactions on Transportation Electrification*, Vol. 9, No. 2, 3218–3227, 2023.

[22] Liu, C., Z. Chao, S. Wang, and Y. Wang, "A quick electromagnetic performance analysis method for permanent magnet claw pole machine based on combined analytical and equivalent magnetic circuit method," *Electrical Engineering*, Vol. 105, No. 3, 1541–1553, 2023.

[23] Xin, Y., Y. Sun, X. Wang, X. Xi, Y. Su, and Y. Yang, "Static torque analysis of micro claw-pole stepper motor based on field-circuit combination," *Micromachines*, Vol. 13, No. 9, 1517, 2022.

[24] Zhu, J., S. Li, X. Guo, H. Nan, and M. Yang, "Analytical calculation of leakage permeance of coreless axial flux permanent magnet generator," *COMPEL — The International Journal for Computation and Mathematics in Electrical and Electronic Engineering*, Vol. 41, No. 1, 172–186, 2022.

[25] Zhang, Y., X. Zhang, J. Ren, S. Yan, L. Wang, X. Pang, W. Liu, and Z. Kong, "Study of electromagnetic characteristics of brushless reverse claw pole electromagnetic and permanent magnet hybrid excitation generator for automobiles," *IEEE Transactions on Energy Conversion*, Vol. 39, No. 2, 1288–1300, 2024.

[26] Min, G. and Y. Xu, "Output power capacity improvement based on three-phase current balance control for the doubly salient electromagnetic generator system," *Energies*, Vol. 16, No. 11, 4298, 2023.

[27] Sathasivam, K., I. Garip, A. M. Althahabi, S. Mohammed, A. I. Alanssari, Y. S. Mezaal, J. M. A. Sulaiman, and T. Alawsi, "An analysis of the design of a low rotational speed permanent magnet generator that uses radial flux," *Electric Power Components and Systems*, Vol. 51, No. 18, 2171–2180, 2023.

[28] Zhao, X., S. Niu, and W. Fu, "Sensitivity analysis and design optimization of a new hybrid-excited dual-PM generator with relieving-DC-saturation structure for stand-alone wind power generation," *IEEE Transactions on Magnetics*, Vol. 56, No. 1, 1–5, 2020.

[29] Qiao, Z., L. Shi, F. Li, H. Xu, T. Zhou, and W. Wang, "Characteristics analysis of magnetic-pole-shift in an asymmetric hybrid pole-permanent magnet assisted synchronous reluctance motor," *IEEE Journal of Emerging and Selected Topics in Power Electronics*, Vol. 13, No. 2, 1394–1405, 2025.

[30] Xu, A., C. Huang, B. Yi, F. Wang, and Z. Liu, "Multi-objective optimization design of surface-mounted and interior hybrid permanent magnet synchronous motor," *Progress In Electromagnetics Research C*, Vol. 154, 239–248, 2025.